Received: 3 November 2021 | Revised: 26 May 2022 | Accepted: 15 July 2022

DOI: 10.1002/mp.15880

RESEARCH ARTICLE

MEDICAL PHYSICS

Comparison of PMT-based TF64 and SiPM-based Vereos PET/CT systems for ^{90}Y imaging and dosimetry optimization: A quantitative study

Nicola Trotta[1] | **Benoît Collette**[1] | **Céline Mathey**[1] | **Irina Vierasu**[1] | **Ana-Maria Bucalau**[2] | **Gontran Verset**[2] | **Rodrigo Moreno-Reyes**[1] | **Serge Goldman**[1]

[1]Department, of Nuclear Medicine, Hôpital Erasme, Université libre de Bruxelles (ULB), Brussels, Belgium

[2]Department of Gastroenterology, Hôpital Erasme, Université libre de Bruxelles (ULB), Brussels, Belgium

Correspondence
Nicola Trotta, Department of Nuclear Medicine, Hôpital Erasme, Université Libre de Bruxelles (ULB), Route de Lennik 808, 1070 Brussels, Belgium.
Email: nicola.trotta@erasme.ulb.ac.be

Abstract

Background: Selective internal radiotherapy based on transarterial radioembolization (TARE) with yttrium-90 (^{90}Y) microspheres is an established treatment for primary or metastatic liver disease.

Purpose: The objective of this work is to optimize the dosimetry of patients treated with ^{90}Y TARE, using positron emission tomography (PET) images.

Methods: The NEMA 2012 PET phantom was filled with nearly 3.9 GBq of ^{90}Y activity and acquired at days 0, 3, 5, 7, and 9 on a classic time-of-flight PET/computed tomography (CT) scanner (Philips TF64) and on a silicon photomultiplier (SiPM)-based PET/CT scanner (Philips Vereos). Acquisitions were carried on following the guidelines proposed in a previously published multicentric trial and images were reconstructed by varying and combining the available parameters. Comparisons were performed to identify the best set(s) of parameters leading to the most accurate ^{90}Y-PET image(s), in terms of activity distribution. Then, for both scanners, the best images were analyzed with *Simplicit*^{90}*Y*, a personalized dosimetry software using multicompartmental Medical Internal Radiation Dose model. The comparison between measured and true doses allowed to identify the image granting the most consistent dose estimations and, therefore, to designate the set of parameters to be applied on patients' data for the reconstruction of optimized clinical images. Posttreatment dosimetry of four patients was then realized with *Simplicit*^{90}*Y* using optimized imaging datasets.

Results: Based on activity distribution comparisons and dose estimations over phantom and patients data, the SiPM-based PET/CT system appeared more suitable than the photomultiplier tube-based TF64 for ^{90}Y-PET imaging. With the SiPM-based PET/CT system, reconstructed images with a 2-mm voxel size combined with the application of the point spread function correction led to the most accurate results for quantitative ^{90}Y measures.

Conclusions: For the SiPM-based PET/CT scanner, an optimized set of reconstruction parameters has been identified and applied on patients' data in order to generate the most accurate image to be used for an improved personalized ^{90}Y-PET dosimetry, ensuring a reliable evaluation of the delivered doses.

KEYWORDS
image reconstruction optimization, personalized dosimetry, positron emission tomography, ^{90}Y-selective internal radiotherapy

Nicola Trotta and Benoît Collette authors contributed equally to this work.

1 | INTRODUCTION

Liver cancer has become a major health problem with a continuously growing incidence over a decade in our countries.[1] Fortunately, the number of therapeutic options is continuously growing too: surgery, simple embolization, radiofrequency ablation, systemic therapy (checkpoint and tyrosine kinase inhibitors), and chemo- and radioembolization are nowadays well-established treatments. Among these therapies, the place of radioembolization remains a subject of debate. Personalized predictive dosimetry improvements are carrying this kind of selective internal radiotherapy (SIRT) to the spotlights; as a matter of fact, past comparative studies without dosimetry have clearly underestimated its potential.[2–4]

SIRT is based on transarterial radioembolization (TARE) in liver cancer treatment, using yttrium-90 (^{90}Y)-labeled microspheres.[5] The effectiveness of TARE depends on the preferential arterial vascularization of liver tumors. Thus, if the lesions are well targeted, TARE delivers a high dose of radiation at the targeted volumes, while sparing the non-tumoral liver parenchyma.[6,7] In the past, ^{90}Y TARE was classified in comparative studies with multikinase inhibitors as a treatment with poor results. The SIRveNIB (SIRT vs. sorafenib) and SARAH (sorafenib versus radioembolisation in advanced HCC [hepatocellular carcinoma]) trials failed to prove a superiority of TARE compared to sorafenib. However, they confirmed the safety and efficacy of this treatment in patients with locally advanced HCC.[2,3] Today, better designed trials are conducted and challenge the interpretation of previously published negative trials of TARE, in which personalized predictive dosimetry was not used.[8]

Prediction of ^{90}Y-microspheres distribution in tumor and non-tumor thanks to the technetium-labeled albumin macroaggregate (^{99m}Tc-MAA) pretreatment imaging improves TARE efficacy.[9,10] Response to ^{90}Y radioembolization is commonly assessed a few months after treatment using conventional anatomical imaging and tumor markers.[11] Precise post-therapy dosimetry could prompt an early evaluation of the response in order to rapidly complement a treatment that is expected to be inefficient, either by a repeated TARE or by the implementation of another type of therapy.

As a pure ß-emitter, ^{90}Y has the advantage of a very localized energy deposition, which avoids harmful irradiation of non-embolized parts of the liver as well as extra-hepatic regions (e.g., stomach, intestines, and lungs) in the context of TARE therapy. In addition, patients can be released shortly after treatment with minimal precautions thanks to the low level of photon emissions and to the absence of free ^{90}Y circulation. However, these advantages come at a cost as direct monophotonic imaging of this radionuclide is not possible. For years, the most common posttreatment imaging in the case of ^{90}Y TARE was therefore indirect, making use of the braking radiation (bremsstrahlung emission computed tomography, BECT), which imposes a large energy window. Unoptimized reconstruction algorithm and collimators' inefficiency for the high-energy X-rays from bremsstrahlung are the principal drawbacks responsible for the low spatial resolution typical of this imaging technique.[12,13] Despite some recent progress,[14,15] BECT images are quantitatively less precise without careful parameter optimization and advanced reconstruction algorithms, making them difficult to use for accurate dose–response analysis.

Positron emission tomography (PET) imaging has been identified for more than a decade as a direct visualization method for the ^{90}Y spread-out distribution of activity delivered by TARE.[16–19] Although ^{90}Y has traditionally been considered a pure β^- emitter, the decay of this radionuclide produces a minor chain to the first stable 0^+ excited state of ^{90}Zr, followed by β^+/β^- emission with a very low branching ratio.[20] Over the last 15 years, it has been proposed to take an advantage of this production of β^+/β^- pairs to assess the distribution of ^{90}Y by PET imaging, especially in regions with high ^{90}Y concentration during therapeutic administration of ^{90}Y-labeled radiopharmaceuticals.

^{90}Y-PET imaging is particularly suitable for posttreatment dosimetry realized right after the ^{90}Y microspheres implantation: in fact, it makes possible to check whether the injection and the fixation of the spheres have been carried out correctly and the tumor well targeted. Several authors have published further uses of ^{90}Y-PET imaging, especially if a time-of-flight (TOF) correction is applied and showed that ^{90}Y-PET produces better quality images than BECT.[16,21] Furthermore, recent progresses in PET technology have made available a new generation of PET/CT scanners providing higher standards of sensitivity and TOF resolution that could particularly benefit ^{90}Y imaging.[17]

The aim of this work is to optimize ^{90}Y-PET imaging and thus the posttreatment personalized dosimetry of patients who underwent TARE therapy with ^{90}Y-labeled glass microspheres. In the context of ^{90}Y-PET imaging, we evaluated the performances of a fully silicon photomultiplier (SiPM)-based Philips PET/CT scanner Vereos (Philips Medical Systems, Cleveland, Ohio, USA) in comparison to its classic photomultiplier tube (PMT)-based counterpart, the Philips TF64, through the acquisitions of a NEMA phantom and quantifications of ^{90}Y-PET images obtained with different reconstruction settings, in analogy with the QUEST study.[22] We then applied the selected parameters datasets in a simulated posttreatment dosimetry carried out with *Simplicit*^{90}*Y* (Mirada Medical, Oxford, United Kingdom), the software currently used in clinical routine, in order to refine the determination of the best parameters dataset. This dataset was

TABLE 1 Activities and days of acquisition of the NEMA phantom

Acquisition days	Δ*t* (h)	Activity @ acquisition time (MBq)
D0 Vereos	6.8	3618.88
D0 TF64	10.72	3469.83
D3 Vereos	77.9	1687.54
D3 TF64	83.52	1588.79
D5 Vereos	127.33	992.92
D5 TF64	132.08	943.59
D7 Vereos	174.33	599.65
D7 TF64	178.72	572.06
D9 Vereos	222.56	357.40
D9 TF64	228	337.13

Note: Activities and days of acquisition of the NEMA phantom for both PET/CT scanners. The second column shows the time between the measurement at injection and the start of the acquisition, the third column the calculated activity (corrected for ^{90}Y decay) at the time of acquisition. On the 5 days of acquisition, the phantom was always acquired on the Vereos scanner and then on the TF64 scanner.

then applied to the ^{90}Y-PET data acquired from four patients treated by ^{90}Y TARE in our institution.

2 | MATERIALS AND METHODS

2.1 | Phantom

The NEMA 2012/IEC 2008 PET phantom consists of a 9.7-L torso-shaped compartment containing six fillable spheres (inner diameter of 10, 13, 17, 22, 28, and 37 mm) and a cold, cylindric lung insert (inner diameter of 51 mm) fixed in the central axis. The phantom was prepared in a similar way as in the QUEST study protocol[22] with a ^{90}Y-chloride solution mixed with diethylenetriaminepentaacetic acid (DTPA). As ^{90}Y is very sticky to the plastic walls of the phantom and especially of the spheres, it was necessary to provide this mix of water and DTPA to avoid this drawback, which could lead to an inhomogeneous distribution of the radioisotope. The entire volume of water used to fill the phantom was supplied by a Merck ICW-3000 water column, providing an ultrapure type 1 water.[23] The purity of the water is important to avoid the growth of bacteria and other impurities in the phantom during the acquisition period.

The phantom was filled with an activity ratio between spheres and background of 8:1, as recommended in the QUEST protocol.[22] The initial injected activity was 3.89 GBq. Acquisitions took place over a period of 10 days. Having set D0 as the day of injection, the NEMA phantom was acquired on both PET/CT scanners at D0, D3, D5, D7, and D9. Table 1 summarizes the activities calculated on the different acquisition days. This timespan allowed to reach a range of activity spanning from 3.6 GBq to around 350 MBq, which is a representative of the ^{90}Y activities mostly used for patients undergoing TARE treatments performed at our institution.

TABLE 2 Technical specifications of the Philips positron emission tomography (PET)/computed tomography (CT) systems

	Vereos	TF64
Crystals—dimensions (mm^3)	LySO—4 × 4 × 19	LySO—4 × 4 × 22
Detector elements	Silicon photomultipliers	Photomultiplier tubes
Axial FOV (cm)	16.4	18
TOF timing resolution (ps)	306.7	616.5
Transverse spatial resolution @1 cm vertically (mm [FWHM])	4.35	4.63
Sensitivity (according to NEMA NU-2 2012) (kcps/MBq)	6.2	7.49
Time coincidence window (ns)	4	6
Energy window (keV)	415–613	440–650
Bed overlap (%)	39	53

Note: Technical specifications of the Philips PET/CT systems, the Vereos and the TF64.
Abbreviations: FOV, field of view; FWHM, full width half maximum; LySO, lutetium–yttrium orthosilicate; TOF, time-of-flight.

2.2 | Image acquisition

For every acquisition, the NEMA phantom was scanned for 2.5 h on both PET/CT systems. The bed positions required to include the entire phantom in the field of view (FOV) were two, so the duration of each bed position was set at 1.25 h. The majority of the measurements presented in the rest of this work were performed over 30 min of acquisition, consisting in the first 15 min of each bed position, as per the QUEST protocol.[22] For each PET scan, a CT scan was made for attenuation correction. Table 2 shows the principal technical specifications of both PET/CT systems. For a detailed

description, see Ref. [24] for the TF64 and Ref. [25] for the Vereos.

2.3 | Image reconstruction parameters—TF64

The default reconstruction protocol of the TF64 system provides an imposed combination of 3 iterations and 33 subsets; this setting cannot be modified by the user. The reconstruction method is iterative, following the BLOB-OS-TF algorithm. This technique takes into account spherically symmetric elements of volume with smoothed values near their boundaries instead of the more conventional voxels for image reconstruction. Their use, instead of voxels, introduces additional parameters that allow the user to control the shape of the volume element (blob) and thus to control the characteristics of the images produced by iteration from the projection data. In theory, images reconstructed using appropriately chosen blobs are characterized by less noise for both noiseless and noisy data, without any loss of resolution in the image. With each iteration, the contrast and sharpness of the image increases but so does the noise, so much that after a certain number of iterations, subsequent iterations add noise without improving the image quality.

2.3.1 | HQ option

The typical iterative reconstruction includes the TOF information, which is characterized by a certain Gaussian distribution. The kernel width is 14.1 cm ($=2\sigma$) for the standard algorithm, but it is possible to choose the "higher quality" (HQ) option, which takes into account an extended Gaussian distribution, with a kernel width fixed at 18.7 cm ($=3\sigma$). Based on the ability of the TF64 system to measure the difference between the arrival times of coincident photons (TOF), allowing for a better positioning of each event, the setting of the kernel width limits the region of space in which the event is positioned. A larger kernel width not only provides a more accurate positioning of each event but also increases the reconstruction time.

2.3.2 | 2-mm option

The default reconstruction protocol uses a 144 × 144 matrix, resulting in a pixel size in the image of 4 × 4 mm^2 (x 4 mm in the axial direction). However, an additional protocol is provided for head-and-neck studies with a 288 × 288 matrix, resulting in a pixel size of 2 × 2 mm^2 (x 2 mm in the axial direction due to blob modeling of the image), thus reconstructing a final image with a half of the default spatial resolution, but extending the process time.

2.3.3 | Reduced energy window (E_{red}) option

Although the operating system installed on the TF64 is Windows-based for the generic user, it is possible to reach a deeper level of software architecture and access its Unix layer. In this environment, command line functions allow one to manipulate the raw PET data (*list* files) acquired. In particular, we were able to exclude from the *list* file the events acquired within a certain energy window set by the user. As explained earlier, given the emission spectrum of the ^{90}Y, it is interesting to reduce the upper limit of the energy window to 550 keV rather than 650 keV as configured by default. The elimination of events acquired at an energy beyond this stricter threshold should avoid taking into account a part of the bremsstrahlung photons emitted by ^{90}Y decay.[26]

2.4 | Image reconstruction parameters—Vereos

2.4.1 | PSF option

In the new Vereos system, Philips has introduced the possibility to integrate the Richardson–Lucy algorithm for image reconstruction. This algorithm incorporates the Poisson statistics, and its form is very similar to the typical iterative maximum likelihood expectation maximization (MLEM) algorithm used in PET, the goal of which is to maximize the likelihood function. The main drawback of the ML approach is that in the presence of noise, the iterations try to fit the data as well as possible. In order to avoid overfitting, some form of noise regularization is necessary. Using the "sieve" method proposed by Snyder and Miller,[27] a regularized version of the Richardson–Lucy algorithm can be used according to the following equation:

$$f_{k+1} = \frac{f_k}{h \cdot s}\left(h \cdot s \cdot \frac{g}{f_k \otimes h \otimes s}\right)$$

where f is the original undistorted image, g is the distorted noisy image, h is the point spread function (PSF) of the system, s is the full width half maximum of the Gaussian sieve kernel used for regularization, k is the number of iterations, and $\otimes$ the convolution operator. This algorithm can be applied on the condition that an accurate measurement of the scanner PSF is provided, which has been accomplished for the Vereos scanner by Philips through a careful measurement of point sources

at many points in the FOV. The PSF implementation allows two parameters to be changed by the user: the number of iterations *k* and the regularization value *s*. As advised by the manufacturer, typically one to two iterations and a regularization value of 6–8 mm provide images with good resolution without introducing excessive noise amplification or quantification errors. As the optimization of these parameters was beyond the scope of this work, the default configuration for the PSF option was confirmed at $k = 1$ iteration and $s = 6$ mm of regularization.[28]

2.4.2 | 2-mm option

As for the TF64 system, reconstruction according to a 288×288 matrix is also available. This provides a final image with a voxel size $2 \times 2 \times 2$ mm^3. As the PET detector is fundamentally different between the two systems (see Table 2), the spatial resolution of Vereos is superior due to several improvements in the detector ring design. The signal-to-noise ratio is the main beneficiary of this improvement at the acquisition level, and this should be accordingly emphasized in a reconstructed image with smaller voxel sizes.

2.4.3 | Iterations/subsets option

Contrary to the TF64 system, it is possible on the Vereos system to modify the number of iterations and subsets of the reconstruction algorithm. The MLEM reconstruction as seen previously requires a few tens of iterations and consequently a very long computation time. So, accelerated versions considering only a subset of the data at each iteration are often used. In the Philips systems, the ordered subset expectation maximization (OSEM) algorithm is preferred, where the number of response lines of response (LOR) is divided into several subsets. Only the detections along the LORs of a subset are computed, compared, and back-projected during an iteration. In each iteration, a different subset is used. The default pair proposed is 3 iterations and 15 subsets but the choice is left to the user, who must nevertheless know the theoretical principle behind these values. Increasing the number of iterations essentially causes an increase in the noise in the reconstructed image, which can distort the quantification and does not produce a better image if the convergence of the algorithm has already been reached (while unnecessarily extending the reconstruction time). Increasing the number of subsets, that is, the subdivision of the data into smaller packets, can be harmful in the case of low count rate acquisition as is the case for ^{90}Y. In this work, we first evaluated the effects of a reduction (2i15s) and an augmentation (3i24s) of the iteration/subset pairs. Then, the choice of a much more radical combination was studied, where the algorithm was brought to convergence after three iterations but with the acquisition data divided into only five subsets. By so drastically decreasing the number of subsets, the size of each subset is large, and each of them contains more tomographic and statistical information. This can be crucial in processing sparse data from a low count statistic, leading to a decrease of noise and other artifacts in the final image.[29,30] Further combinations of iterations/subsets are still possible but in this work only four OSEM settings have been investigated. Moreover, we choose not to decrease subsets to a value lower than 5 as advised by the manufacturer for ^{90}Y imaging.

2.4.4 | Reduced energy window (E_{red}) option

In the Vereos system, the Unix layer was unfortunately inaccessible, thus making impossible to use the command line tools as in the TF64 system to work on raw *list* files. Despite that, we were able to recover, export, and read the original *list* files related to the NEMA phantom acquisitions thanks to a Matlab toolbox provided by Philips. A Matlab code was then developed to exclude the events acquired in a specific energy window set by user (Matlab 9.2 R2017a, MathWorks Inc., Natick, MA, USA). The upper limit of this window, originally configured at 613 keV, was reduced to 550 keV in order to remove most of the noise from the ^{90}Y bremsstrahlung radiation.

2.5 | Data quantification

For each PET acquisition, the corresponding CT acquisition was realized and used for image co-registration and 511-keV photon attenuation correction. The CT data were also used to segment the six spheres within the phantom into 3D volumes of interest (VOI) using a semiautomated region growing algorithm to delineate the physical volume of the sphere. PMOD version 3.8 was used for this task (PMOD Technologies, Zurich, Switzerland). Following the methodology developed in the QUEST study,[22] in this work we chose to quantify three indicators in order to obtain measures of activity or activity concentration in the VOIs.

- The total activity in MBq in the reconstructed FOV, in order to have an indicator of the global activity injected into the phantom. Values were expressed at first as a relative difference between the activity measured in the image and the actual activity injected, and then as a ratio between these two activities calculated over seven acquisition times (10′, 20′, 30′, 60′, 90′, 120′, and 150′) for each of the time points indicated in Table 1. This is intended to give an insight

into the ability of the PET/CT scanners to reproduce in the image a satisfactory estimate of the true activity, by investigating the behavior of the system over acquisition times longer than those used in clinical routine.

II The average activity concentration for each of the spherical VOIs defined in the CT image applied to the PET images, in order to calculate the associated recovery coefficient (RC) to assess the partial volume effect (PVE) on the data acquired at D0. The RC is typically defined as the ratio of the measured volume activity to the actual volume activity in MBq/ml according to the following equation:

$$RC\,(\%) = \frac{measured\ activity\ concentration}{true\ activity\ concentration} \times 100$$

The potential of PET imaging to produce quantitative measurements of tracer concentrations is severely impacted by the PVE,[31] which leads to unreliable quantitative values, especially for small volumes, as well as poor image quality. Indeed, PVE can be seen as a contamination of the intensity distribution, causing the signal in areas of higher uptake (e.g., a tumor) to spill over into areas of lower uptake. The presence of PVE is a direct result of the limited spatial resolution of PET imaging, which in turn is a consequence of several independent factors. These include the path of positrons in the tissue prior to annihilation, the non-collinear path of photons from annihilation (due to momentum conservation in the β^+/β^- system), the mean free path of the photon in the detector prior to absorption, the energy resolution of the detector, and the reconstruction filters applied.

These coefficients, as defined, theoretically allow the actual activity value to be "recovered," using the specific RC for the size of the region of interest investigated in the image. The evolution of the RCs associated with the largest diameter sphere (37 mm), which is the least affected by the PVE, was also evaluated on the different days of acquisition in order to confirm the link between recovery and deterioration of the counting statistics.

III Misplaced activity in the central "cold" cylindric insert is the calculated average in a central ROI replicated on five cross sections in the cylinder as a percentage of the actual concentration in the phantom. This measurement provided an index of the signal in the phantom (background) that could be measured in adjacent supposedly cold regions. This reflects the "hot-to-cold" spillover due to PVE noticeable in a PET image, which may lead to an overestimation of the absorbed dose in healthy liver regions, possibly devoid of any activity deposition. Recent studies have investigated the difficulty of assessing the impact of scattered and random events in ^{90}Y-PET data against actual activity fixation in non-targeted regions, but no true quantitative solution has been proposed.[32] In this context, we plotted the activity profile across regions of interest placed inside the cold cylinder, in order to compare the behavior of PET/CT scanners about the dispersion of activity and to evaluate which one is the best to correct these misplaced events.

These quantifications were repeated on every image generated by tuning the parameters of the reconstruction algorithms, as previously described. This method made it possible to investigate a vast range of parameter combinations and, thus, to provide different PET images, which were more or less representative of the reality. The aim was to determine the best sets of parameters that assure the reconstruction of ^{90}Y-PET images reproducing the activity distribution as accurately as possible. Then, in order to approach a more clinical situation, the selected images were used as input to the dosimetry software, *Simplicit^{90}Y*. By a relative multi-compartmental method, following the Medical Internal Radiation Dose (MIRD) model, on the basis of the total injected activity (in GBq), the software was able to estimate the dose distribution between the compartments and to deduce the mean delivered dose in the VOIs considering a conversion factor for liver tissues (in Gy). Nevertheless, the model is based on the assumption of a uniform distribution of the ^{90}Y microspheres,[33] whereas, in reality, their distribution is quite heterogeneous. This assumption is then acceptable only as an approximation. Hence, providing as input a PET image with the most accurate ^{90}Y activity distribution was crucial to obtain the most reliable results in terms of dosimetry.

It was therefore necessary to prove that the choice of parameters for the reconstruction of the ^{90}Y-PET image was quantitatively as suitable as possible. The error introduced in terms of activity distribution in the image used could be taken into account for the dose estimation. To do this, at first, the mean dose in Gy estimated by the software in the spheres of the phantom were compared to the "true" dose calculated using the true activity injected in the same spheres and the well-known conversion factor for liver tissues.[34] This "dose ratio" (DR) was calculated on each image and for each sphere considered individually according to the following equation:

$$DR\,(\%) = \frac{measured\ dose}{true\ dose} \times 100$$

This ratio should be considered an index of reliability that the chosen combination of reconstruction parameters gave the best response in terms of dosimetry and could therefore be applied to patients' data in the next step.

TABLE 3 Patients selected

Patient	Gender	Age	Pathology	Lesion size	Liver segment	Injected ^{90}Y activity (GBq)
1	F	84	Cholangiocarcinoma	21 mm	VIII	0.51
2	M	63	Hepatocarcinoma	16–13–8–6 mm	VI	0.39
3	M	77	Hepatocarcinoma	16 cm	VIII	7.32
4	F	85	Cholangiocarcinoma	35–8 mm	IVb/V	1.26

Note: Demographics and pathology characteristics for each included patient.

TABLE 4 Images retained after the quantifications

TF64		Vereos	
Image	Reconstruction	Image	Reconstruction
1	default	1	Default
2	HQ	2	PSF 2 mm
3	HQ E_{red}	3	PSF 2 mm E_{red}
–	–	4	3i5s 2 mm
–	–	5	3i5s 2 mm E_{red}

Note: Images retained based on the results of the quantifications. For the TF64 scanner (left-hand columns), we selected the images reconstructed with default parameters (1), HQ option (2), and reduced energy window with HQ option (3). For the Vereos (right columns), we selected the images reconstructed with default parameters (1), combination of PSF and 2-mm voxel size (2), reduced energy window with combination of PSF and 2-mm voxel size (3), three iterations/five subsets and 2-mm voxel size (4) as well as reduced energy window with 3i/5s combination and 2-mm voxel size (5).
Abbreviations: HQ, higher quality; PSF, point spread function.

2.6 | Patient selection

In a real clinical context, we selected cases of unresectable liver cancer included in the ^{90}Y TARE treatment protocol of the gastroenterology department of our institution. Of the four patients included in this analysis, two cases presented HCC and the other two intrahepatic cholangiocarcinoma, with lesions of different sizes positioned in different segments of the liver. Table 3 summarizes the characteristics of the patients included, detailing position and size of each lesion.

For all four patients, data were acquired successively on both PET/CT scanners, right after the TARE was realized in the interventional radiology suite. The acquisitions covered two overlapping bed positions centered on the liver (20 min per bed[34]), and posttreatment dosimetry was performed with *Simplicit*^{90}*Y* already used for the phantom analyses. The co-registration of PET images with structural magnetic resonance imaging (MRI 3D-T1 sequences) was performed via rigid registration with *Simplicit*^{90}*Y*. Because of the poor accuracy with the automatic process of co-registration in this software, we applied the manual rigid PET/MRI co-registration procedure that was double-checked by two physicists and validated by a physician. The lung shunt fraction was visually confirmed to be neglectable on a bremsstrahlung emission whole-body scan and set to 0, whereas the segmentation of the liver and VOI was performed manually on the MRI. We focused on dose estimations in the perfused tumor volume. We realized a comparative analysis of the dosimetric results using the default ^{90}Y-PET image reconstructed by the PET/CT system and using the image obtained through the optimized reconstructed parameters, in order to highlight the differences in terms of dose estimation absorbed by the tumor lesions in the perfused liver volume. The results obtained for the patients were also related to the results obtained from the phantom data to verify if the differences between the images considered in the dosimetric analyses were reproductible. The analysis of data acquired on the PET systems for clinical indications has been approved by the Ethics Committee of the institution, which waived the obligation of written informed consent.

3 | RESULTS

Following the quantification index I, the relative differences between the total activity measured in the FOV and the total activity expected for the five acquisition points in time are presented in Figure 1. Parts (a) and (b) of the figure show the relative differences, respectively, obtained for the TF64 and Vereos scanners using different reconstruction parameters and their combinations as previously described (see the figure legend). Moreover, Figure 2 shows the graphs of the activity ratios calculated for different acquisition times of the NEMA phantom (10′, 20′, 30′, 60′, 90′, 120′, and 150′ for each acquisition day). Due to the amount of data, we decided to show here only the ratios obtained for the image reconstruction with a voxel size of 2 mm for both systems.

The RCs of the hot spheres (index II) obtained for the D0 acquisition is shown in Figure 3, varying the reconstruction parameters for both PET/CT systems. Graph A in the figure shows the quantification results for the TF64 scanner. Graphs B and C show the combinations for the Vereos scanner in the original and reduced energy window cases (again, only some of the combinations in B are proposed in C). The best interpolation curve is represented by the equation (1):

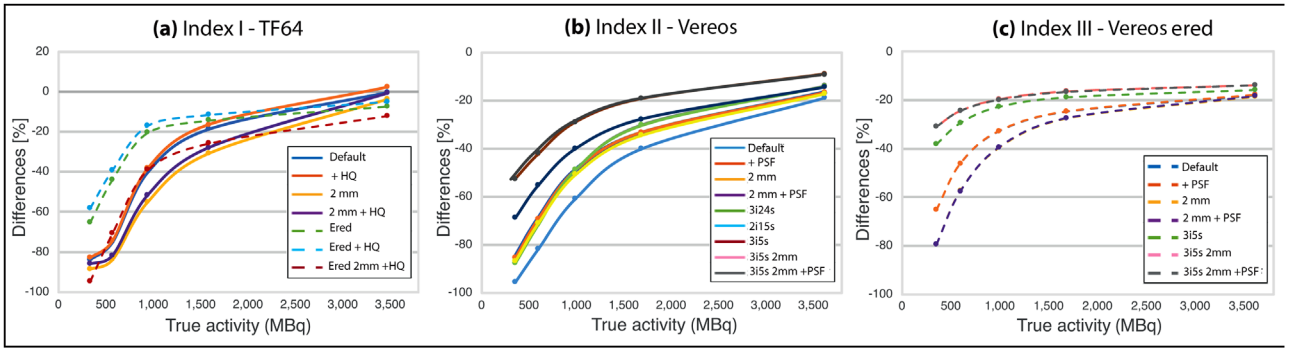

FIGURE 1 (a) TF64: relative differences (index I) obtained with the default reconstruction of the system (3 iterations combined with 33 subsets) without any further changes at first (blue), then with the higher quality (HQ) option selected (orange), with a voxel size of 2 mm (yellow), and with the combination of these two options (violet). Dashed lines show the relative differences with the reduced energy window (green), the combination of a reduced energy window first reconstructed HQ mode (light blue) and with HQ + 2 mm voxel size (red). (b and c) Vereos: (b) relative differences (index I) obtained with the default reconstruction of the system at first (blue), then with the PSD option selected (orange), with a voxel size of 2 mm (yellow), and with the combination of these two options (violet). Different combinations of iterations/subsets are also shown (3i24s in green, 2i15s in light blue, 3i5s in red, 3i5s combined with 2-mm voxel size in rose, and with 2 mm + point spread function [PSF] in gray). (c) Relative differences (index I) obtained with the reduced energy window. Note that only some of the combinations shown in (b) are shown here because the combinations giving poor results with the original energy window are already excluded.

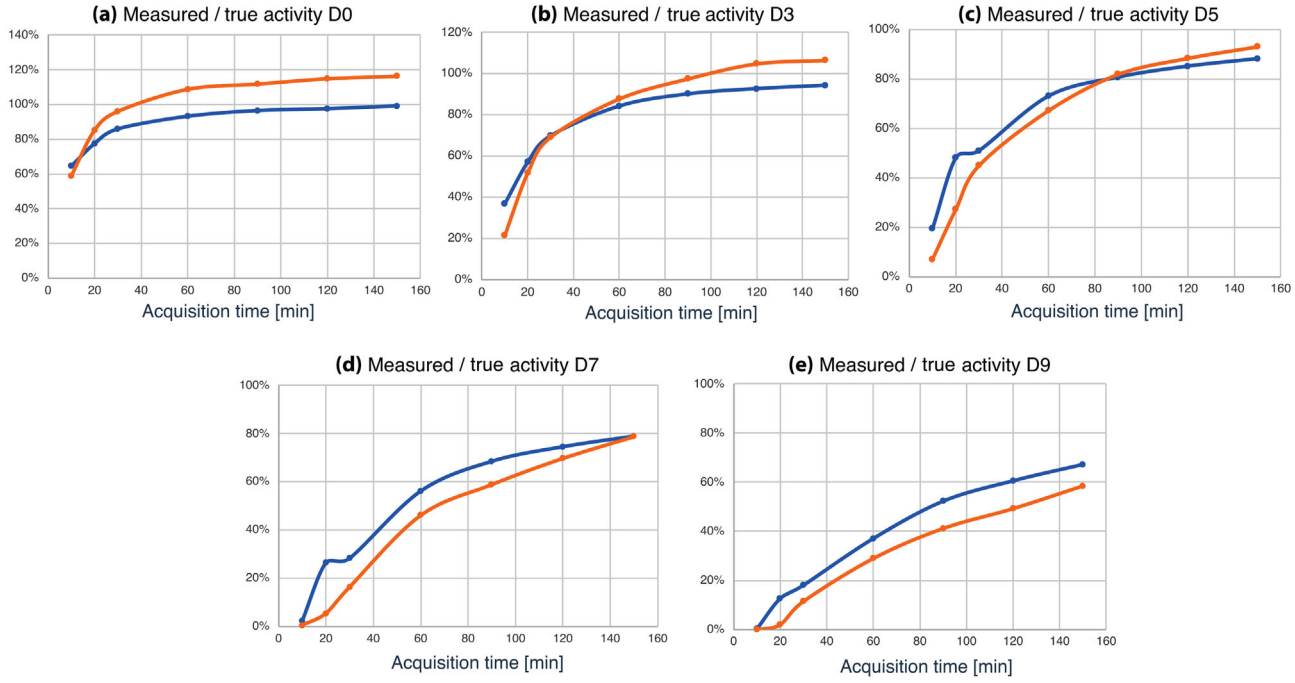

FIGURE 2 Ratios between measured and true activity for the five acquisitions (a: D0, b: D3, c: D5, d: D7, and e: D9) performed on the TF64 (orange) and Vereos (blue) scanners, calculated on images reconstructed over different acquisition times (10′–150′). Only the quantifications obtained on images reconstructed with a voxel size of 2 mm are shown.

$$y = 100 - ae^{-bx}$$

which was calculated for each set of reconstruction parameters used.

The measured activity concentrations in the cold insert (index III) are displayed in Figure 4 as percentages of the actual background concentrations for the different imaging days. The same division of the results into graphs A, B, and C explained for the other quantifications has been adopted here. Figure 5 shows the cross-sectional activity profile in the "cold" cylinder in the center of the NEMA phantom. For purpose illustration, we chose to represent the profiles of the reconstructed images in 2 mm for both systems, taking care to consider the same transverse section for both.

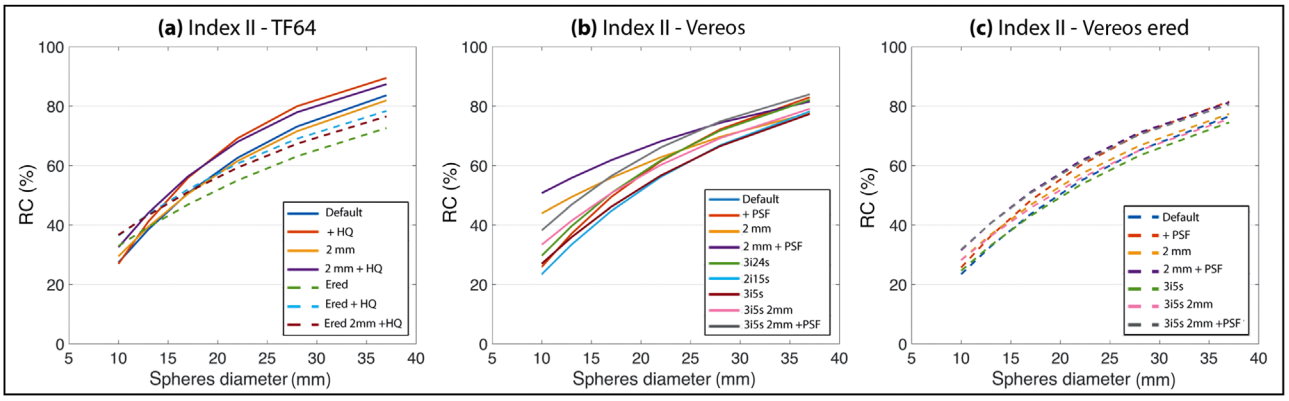

FIGURE 3 (a) Interpolation curves of the recovery coefficient (RC) (index II) for the six spheres of the phantom for the D0 acquisition performed on the TF64 scanner ($0.86 < R^2 < 0.99$), (b) on the Vereos scanner with the original energy window ($0.86 < R^2 < 0.98$), and (c) on the Vereos scanner with the reduced energy window ($0.83 < R^2 < 0.99$). The same reconstruction parameters and their combinations as those shown in Figure 1 (with the same color identification) are presented here.

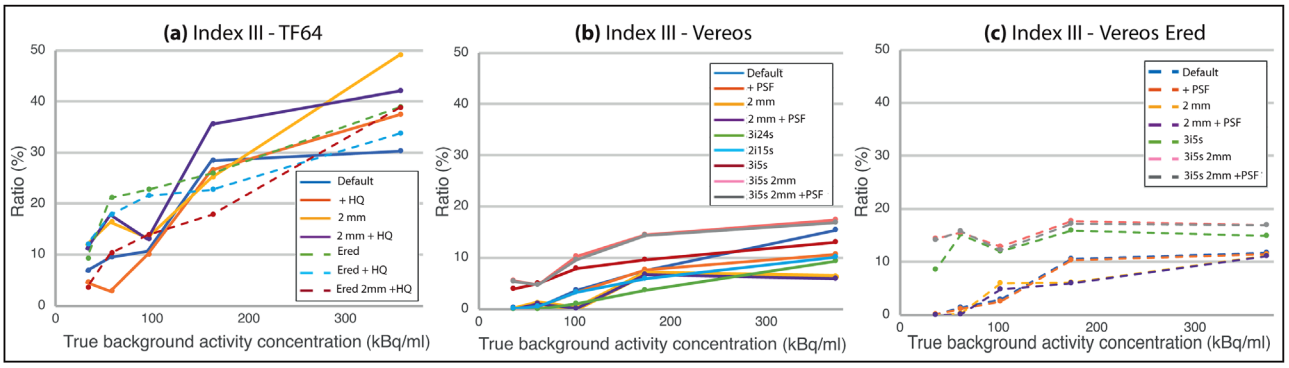

FIGURE 4 (a) Ratios between measured and actual background concentration (index III) for the five acquisitions on the TF64 scanner, (b) on the Vereos scanner with the original energy window, and (c) on the Vereos scanner with the reduced energy window. The same reconstruction parameters and their combinations as those shown in Figure 1 (with the same color identification) are presented here.

Based on these quantification results, five images were retained for the Vereos system and three for the TF64. The reconstruction parameters (or their combinations) that allowed them to be achieved are resumed in Table 4. Our choice was primarily driven by the results obtained for the RCs (index II): The graphs in Figure 3 gave a first hint about which sets of reconstruction parameters were the most promising, that is, the sets that could led to ^{90}Y images reproducing the concentration estimated in each sphere of the phantom as accurately as possible. The results obtained from the other two indexes were also taken into account to corroborate that the choice was still coherent in terms of total activity in the FOV (index I) and misplaced activity in the "cold" central insert (index III).

All these images were then processed in *Simplicit*^{90}*Y* for dosimetry. Table 5 presents the ratios between the dose estimated by the software in the phantom spheres and the dose calculated according to the true activity injected in the same spheres (DR), based on MIRD approach calculation and the theoretical dimensions of the spheres, considering the factor for liver tissues as well.

Figure 6 shows, for each image, the best interpolation curve according to Equation (1) for the DRs obtained for each of the six spheres of the phantom considered individually and listed in Table 5. Graph A shows the results for the three images selected for the TF64, whereas Graph B shows the results for the five images of the Vereos. Figure 7 compares only the set of reconstruction parameters that provided the image on which the best quantitative result in terms of DR was obtained for each of the two PET/CT systems, that is, the image reconstructed with the HQ option for the TF64 scanner and the one reconstructed with the combination of PSF correction and 2-mm voxel size for the Vereos scanner (Figure 8). This last result allowed the comparison of the performance of each scanner for dosimetry based on PET/CT acquisition of patients treated with ^{90}Y-labeled glass microspheres.

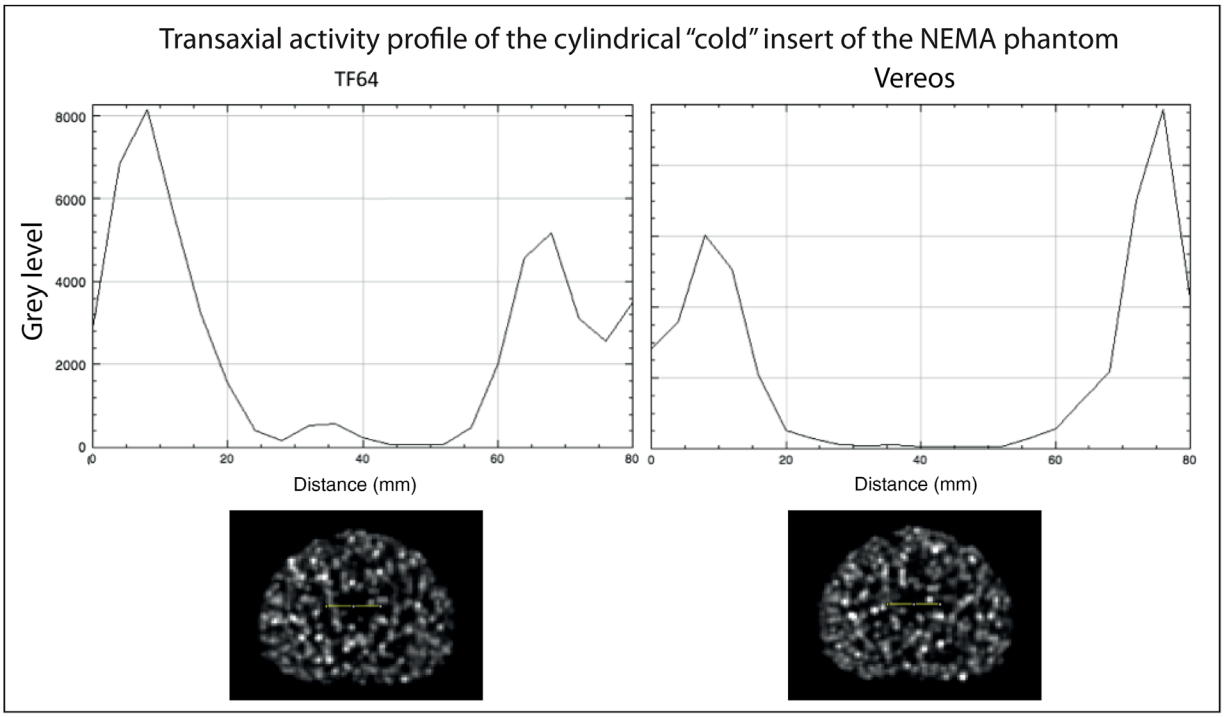

FIGURE 5 Transverse activity profiles in the "cold" cylinder at the center of the NEMA phantom, obtained for the acquisitions on both systems (left, TF64; right, Vereos). Images were reconstructed with a voxel size of 2 mm for both systems, and the same transverse slice was selected. In the lower figure, the cross-section transaxial to cold insert

TABLE 5 Dose ratios estimated for the six spheres of the NEMA phantom

Sphere ϕ (mm)	DR on TF64 images			DR on Vereos images				
	Default	HQ	HQ E_{red}	Default	PSF 2 mm	PSF 2 mm E_{red}	3i5s 2 mm	3i5s 2 mm E_{red}
10	38.57	39.66	40.83	17.40	36.49	27.82	21.53	18.31
13	32.44	33.90	27.34	46.34	59.13	34.74	43.06	45.15
17	46.88	50.45	53.15	48.44	61.86	55.29	59.20	56.48
22	64.37	69.18	69.18	62.42	65.78	76.96	59.97	58.02
28	73.41	78.81	73.05	74.44	96.18	90.94	77.73	77.03
37	91.13	95.50	89.96	97.09	91.15	92.13	85.70	84.51

Note: DRs between the dose estimated by *Simplicit*^{90}*Y* in the six spheres of the NEMA phantom (diameters indicated in the first column on the left) and the dose calculated according to the true activity injected in the same spheres, calculated for each image selected for both systems (see Table 4).
Abbreviations: DR, dose ratio; HQ, higher quality; PSF, point spread function.

The DR values of every phantom sphere used for the interpolated curves showed in Figure 7 have been exploited in order to have an insight on data variability for both scanners, using the statistical technique of bootstrapping. Hence, six new curves were generated by discarding the value of one sphere at a time. For the sets of data of each sphere, we then realized a nonparametric statistic test (Wilcoxon signed-rank test) over the null hypothesis that the distribution of these data has a median = 0. The p-value obtained indicates that the null hypothesis cannot be rejected for the smallest sphere (diameter = 10 mm, $p > 0.05$), whereas it can be rejected for all the other spheres ($p < 0.05$).

For each PET/CT system, the set of reconstruction parameters that gave the best relative quantification in the dosimetric analysis seen in the previous step (as shown in Figures 6 and 7) was applied to the ^{90}Y-PET data of four patients (see characteristics in Table 3). For each patient, Table 6 presents the doses delivered to the perfused tumor volume by analyzing the default image provided by the scanner and the optimized image obtained with the retained set of reconstruction parameters. Figure 9 shows an example of the personalized dosimetry realized with *Simplicit*^{90}*Y* on the images of patient 4, including isodose curves across the liver volumes targeted for treatment, to show changes in

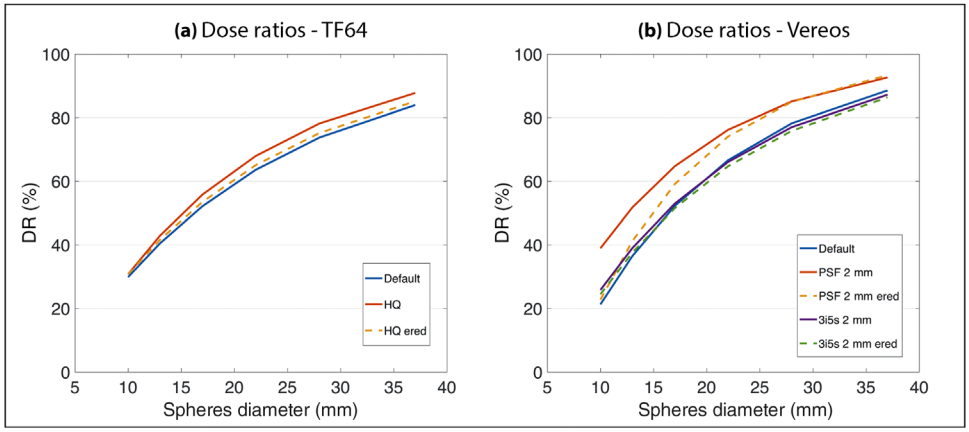

FIGURE 6 (a) Interpolation curves of dose ratios (DRs) for the six spheres of the phantom for the D0 acquisition on the TF64 scanner ($0.85 < R^2 < 0.98$) and (b) on the Vereos scanner ($0.85 < R^2 < 0.98$). Images are reconstructed according to the parameters presented in Table 4.

TABLE 6 Doses delivered to the tumor volumes of the patients

	TF64 images			Vereos images		
Patients	**Default**	**HQ**	**Difference (%)**	**Default**	**PSF 2 mm**	**Difference (%)**
1	360.9	369.1	20.3	305.9	354.1	15.8
2	224.0	248.1	10.8	270.5	323.2	19.5
3	283.6	292.7	3.2	302.8	327.8	8.3
4	707.5	823.7	16.4	910.8	1016.1	11.6

Note: Doses (Gy) delivered to the perfused tumor volumes estimated by *Simplicit*^{90}*Y* on the default and the optimized images for the four patients included. Relative differences between the two measures are showed for comparison between default and optimized image.
Abbreviations: HQ, higher quality; PSF, point spread function.

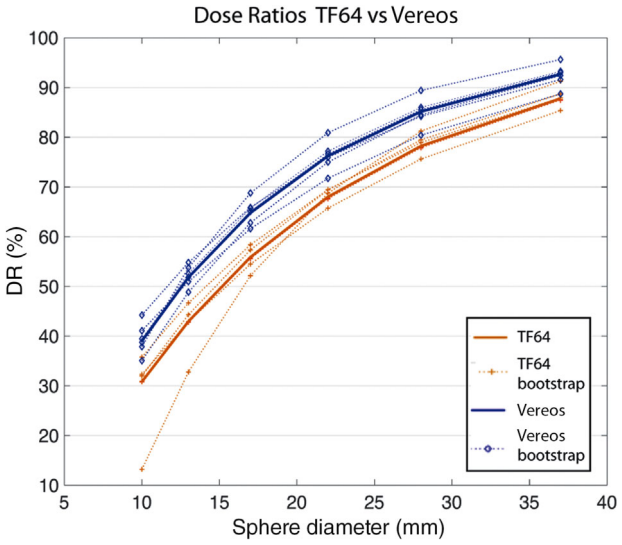

FIGURE 7 Interpolation curves of dose ratio (DR) for the images with the best quantitative dosimetric results (see Figure 6). For TF64 (solid line orange), the image is reconstructed with the higher quality (HQ) option. For Vereos (solid line blue), the image is reconstructed with the combination of point spread function (PSF) and 2-mm voxel size. Dotted curves are the interpolation curves of DR generated for each scanner with the bootstrapping statistical technique in order to test data variability (orange, TF64; blue, Vereos).

the dose distribution estimate depending on the image used for analysis.

The relative differences between the doses delivered to the perfused tumor volume estimated on the default and the optimized images, for all four patients, are comparable between the two scanners (Table 6). Therefore, we pooled them and realized a non-parametric statistic test (Wilcoxon signed-rank test) over the null hypothesis that distribution of these data has a median = 0, that is, no effect can be found in terms of dose estimation over the optimized images compared to the default images. The p-value obtained ($p < 0.05$) indicates that the null hypothesis can be rejected; hence, there is a significant effect in dose estimations due to the use of an optimized image over the default one.

4 | DISCUSSION

This work aimed to compare the new Philips SiPM-based PET/CT system Vereos with the classic PMT-based TF64 system for ^{90}Y imaging.

Concerning the total activity measured in the FOV (Figure 1), relative differences found along the

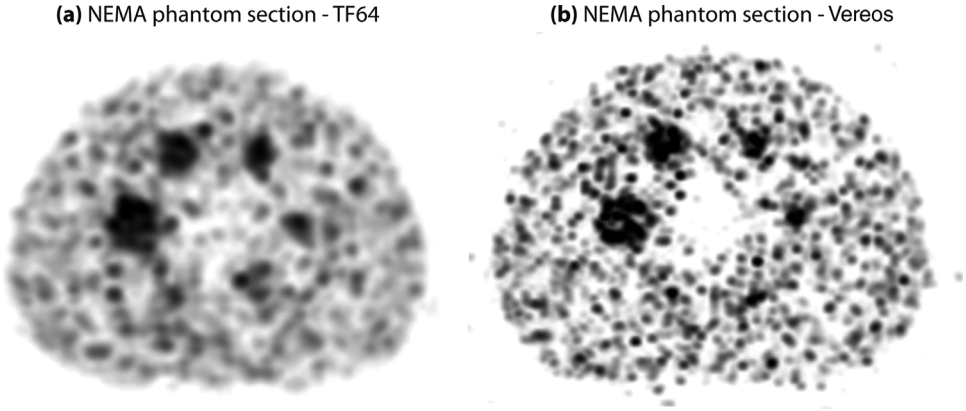

FIGURE 8 (a) Section at the spheres level for the TF64-optimized image reconstructed with the higher quality (HQ) option and (b) section at the spheres level for the Vereos-optimized image reconstructed with the combination of point spread function (PSF) and 2-mm voxel size

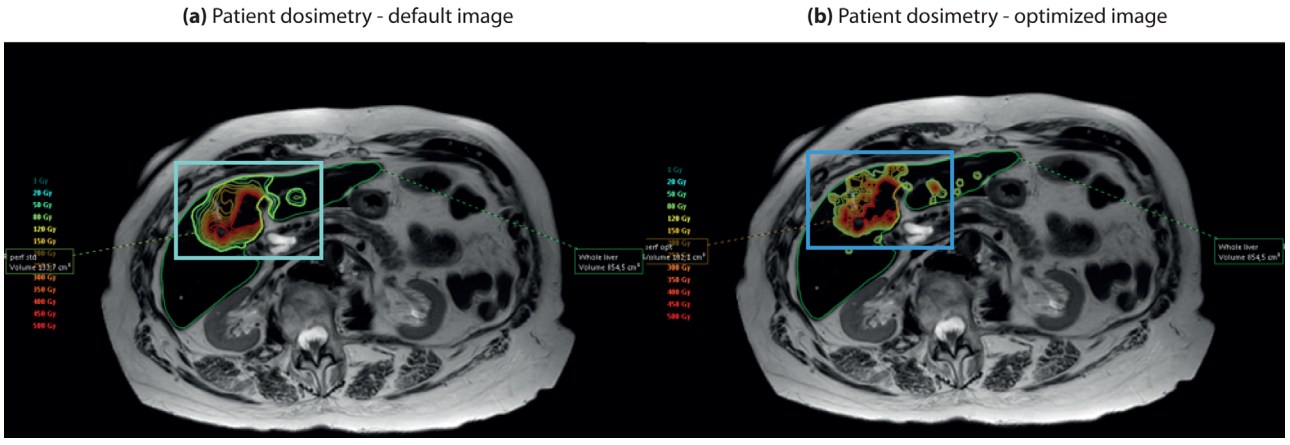

FIGURE 9 Example of a dosimetric analysis performed with *Simplicit*^{90}*Y* on patient 4 treated with ^{90}Y transarterial radioembolization (TARE) (positron emission tomography [PET] acquisition performed on Vereos scanner, (a): default image, (b): optimized image). Highlighted in the frames on the magnetic resonance imaging (MRI) used for segmentation, the perfused tumor volume that is treated and the isodose curves estimated by the software

acquisition period for the TF64 scanner are in agreement with those published in the QUEST study. Indeed, a large underestimation (60%–80%) of total activity is flagrant for small amounts of injected activity (roughly below 2 GBq), whereas reduced differences (20% to 10%) are observed for injected activities up to 3 GBq. The Vereos system, the performances of which, to the best of our knowledge, have not yet been investigated for ^{90}Y, shows smaller differences overall. The discrepancy between the two scanners is little at high activity levels but becomes evident as activity decreases. At last day of acquisition (D9), with residual activity in the phantom at around 300–350 MBq, the difference between true and measured activity on the Vereos images is much smaller than that found on the TF64 images. This ability to better estimate the total activity especially at low range is likely due to the important role played by the method used for the correction of scattered coincidences. For the TF64, this underestimation may be due to the classical *tail fitting* approach,[35] which zeroes prior to subtraction any negative pixels in the scatter-subtracted sinogram. This approximation of the final scatter estimation is then incorporated at the last iteration of reconstruction. Hence, the erroneously high scatter contribution leads to lower counts at low count rates. A hybrid method that combines single scatter simulation (SSS) and Monte Carlo simulations has instead been implemented in the Vereos system.[36] It exploits the typical SSS to approximate the scattered radiation contribution and scales the obtained scattered sinogram with a normalization factor determined by a low-count Monte Carlo simulation, which uses the same activity and attenuation maps as input to obtain the fraction of scattered coincidences. This process takes into account all detected coincidences; it is therefore less noisy than the standard tail fitting approach using only coincidences detected outside the object. By this approach, we also calculate the normalization factors completely

independently of the scattered sinogram, leading to a more robust estimation than the classic method.

By varying and combining the available reconstruction parameters, the best result for the whole range of scanned activity was obtained for both systems in the reduced energy window conditions. Indeed, we can speculate that decreasing the upper limit of the window probably eliminates some of the noise coming from the ^{90}Y bremsstrahlung radiation as well as the natural ^{176}Lu γ-emissions from the crystals, thus improving the signal-to-noise ratio. Furthermore, the smallest difference between true and measured activity is obtained with the HQ option activated for the TF64 and with the three iterations/five subsets combined with a voxel size of 2 mm for the Vereos (Figure 1). For TF64, the use of a larger kernel to measure the difference in the photons arrival time at the detectors allows a better spatial position of each recorded event and, consequently, a better estimation of the activity present in the phantom. For the Vereos system, the use of a smaller number of subsets in the iterative reconstruction makes it possible to distribute the low count rate of a ^{90}Y acquisition as conveniently as possible. Given the very low number of events recorded compared to other isotopes such as ^{18}F, the use of a reduced number of subsets could limit the increasing noise from one iteration to the next, which is confirmed by the worst quantitative result obtained with the 3 iterations/24 subsets combination. Moreover, in contrast with the conventional PMT-based TF64 scanner, the reconstruction of Vereos data with a voxel size of 2 mm benefits from 1:1 crystal-to-SiPMs coupling, making it possible to bypass the Anger logic and to avoid the distortion correction that has an impact on the final spatial resolution of the image. In addition, as the crystals are shorter (19 vs. 22 mm), the resulting TOF is improved as the photons interact in a shallower depth. The diameter of the detector ring is also smaller and the non-collinearity error on the two coincident photons is reduced. Indeed, besides the default image, the four other Vereos images that gave the best quantitative results were all reconstructed with a voxel size of 2 mm. Furthermore, considering long acquisition times (Figure 2), for high activities, the TF64 tends to overestimate the activity, whereas the Vereos often shows a slight underestimation that remains however within a 10% tolerance. As the activity decreases, that is, throughout the acquisition period, both systems show a clear underestimation of the true activity, but the Vereos, especially starting from D5, provides better ratios between measured and true activity. This behavior, particularly visible at longer acquisition durations, highlights the capacity of the Vereos to provide a better performance in the estimation of total activity at lower injected activities.

Few other studies have investigated the impact of scan length on quantification on ^{90}Y-PET images.[37,38] One of them,[37] based on phantom and patients' data, concluded that an acquisition time of 15 min per bed position is adequate for posttreatment dosimetry, showing that ^{90}Y images are too noisy at shorter times, whereas quantification analyses did not benefit from longer acquisition times. Our results are in agreement with this study, as shown in Figure 2 where measured/true activity ratios are clearly insufficient for 10-min scan durations. Higher ratios are yet obtained by increasing the acquisition time to 20–30 min, even at lower activities, and they further rise until plateauing at longer durations. Hence, analyses of phantom data support the choice of 20 min per bed position for patient acquisitions, a timing adopted as an acceptable compromise between image quality and clinical constraints. Incidentally, this duration happens to be recommended by the EANM guidelines. In accordance with this recommendation, a recent study on an SiPM-based PET/CT scanner concluded that an excellent image quality for patients is obtained with a 20-min scan time for a single bed position.[39]

About the quantifications restricted to specific areas of the phantom, that is, the activity concentration measured in the "cold" insert and the RCs for the six "hot" spheres (Figures 3 and 4), the best TF64 image is obtained as before with the application of the HQ option. The increase of the kernel width and, consequently, the ability to better positioning the events, leads to a real benefit in the activity estimation for the hot VOIs as well as for the cold region of the phantom. On the other hand, the reduction of the voxel size to 2 mm does not contribute to any improvement because the signal acquisition technique used in this analog scanner still imposes physical limits to the reconstruction. Similarly, the application of the reduced energy window does not provide a clear gain over the entire range of activity considered, neither in terms of relative difference for the cold insert nor for the RCs of the hot spheres. On the Vereos, the best results can be obtained with a 2-mm reconstruction combined with the application of the PSF correction. For regions of limited size, the higher the spatial resolution of the image, the more accurate the RCs for the hot spheres are. Again, the 1:1 coupling between detectors and SiPM plays a major role. The smaller transverse FOV (76.4 vs. 90.3 cm) and the higher number of photomultipliers (23 040 SiPM vs. 420 PMT) are also crucial to ensure an improved spatial resolution of the Vereos system compared to the previous PMT-based scanner.

Furthermore, for the activity concentration in the cold insert, it is interesting to note the evolution of the activity profile taken on a transverse section of the image (Figure 5). For the TF64, we notice a "blurred" drop in activity at the extremities of the cold insert, characterized by a mild slope. This could be interpreted as a sign that a relatively large number of events are misplaced in the image, then representing false positives, and could lead, on patient data, to errors in

quantifying the dose actually delivered to non-targeted liver parenchyma. For the Vereos, this drop in activity at the border between hot and cold zones is much sharper and reflects its better capacity to assign the detected events to the correct spatial location. Indeed, very few coincidences are interpreted as being inside the cold insert, which is better representative of the reality of the phantom and, therefore, leads to more accurate dosimetry.

Analyses of the NEMA phantom images performed with *Simplicit^{90}Y* show that, among the five sets of reconstruction parameters selected for the Vereos system, the best dosimetric estimation is obtained with a 2-mm reconstruction combined with the application of the PSF correction (Figure 6). It is worthwhile to stress that this type of reconstruction gave the best result in terms of hot spheres' RC, corroborating the link between the best possible activity recovery in hot spots and the most robust estimate of the dose delivered to them. Concurrently, the three iterations/five subsets combination for the OSEM algorithm minimized the discrepancy between measured and theoretical activity in the image (Figures 1b–4b). Nonetheless, this combination of parameters does not produce the same effect in terms of DR (Figure 6b) probably because dose estimation in *Simplicit^{90}Y* is relative and not impacted by the total number of counts present in the phantom, therefore conferring it a limited effect on the dose estimation. Similarly, the use of the reduced energy window does not provide a notable improvement to DR, probably because the Vereos scanner is configured with a stricter energy window (upper limit adjusted to 613 keV compared to the typical value of 650 keV), thus already eliminating a substantial part of random events. Further narrowing of the window would then become unnecessary, as the number of residual events is too low to have any consequence on the estimation of the delivered dose. For the TF64 scanner, among the three parameter sets considered, the best DR was obtained with the application of the HQ option, which is in agreement with the previous quantitative results.

Based on the analyses of the NEMA phantom data, the quantitative comparison of the best set of parameters identified for each scanner shows small differences between the two PET/CT systems. The statistical comparison indicated that these slight differences are significant, leading to the conclusion that the SiPM-based Vereos system can be considered more suitable than the PMT-based TF64 for ^{90}Y-PET imaging and dosimetry (Figure 7).

Dosimetric analyses of patients' images allowed us to evaluate the differences in the estimations of the doses delivered to the targeted volumes, by comparing the standard and the optimized images provided by both scanners. Based on the perfused tumor volume, it is striking that the differences in terms of estimated dose on the patient images go systematically in the same direction as those obtained on the phantom images for the same reconstructions. The precise value or size of these differences between the two datasets is inevitably unobserved, as patients are more complex "objects" being characterized by a higher number of variables than a rigid, static phantom with preset dimensions. Nevertheless, a statistically significant effect on dose estimations has been highlighted with the use of an optimized image compared to the default one. To the best of our knowledge, there is no other published work that investigates PMT- and SiPM-based PET/CT scanners for ^{90}Y imaging in terms of estimated dose. Very recent studies[39,40] compared PMT- and SiPM-based PET/CT scanners from Siemens. The analyses were realized following the protocols suggested in the QUEST study and only concerned data from a NEMA phantom. They did not translate any of their data into a clinical context, and they did not include clinical data in their study.

Our results on patients' data corroborate the quantitative analyses carried out on the NEMA phantom. They confirm that the Vereos system is more appropriate than the TF64 for ^{90}Y-PET imaging of patients. In the context of a posttreatment personalized dosimetry, we recommend reconstructing ^{90}Y-PET images acquired on the Vereos system with a 2-mm voxel size combined with the application of a PSF correction.

This study has some limitations. The total volume of the NEMA phantom is not representative of the volume of a human liver, especially in pathological conditions. Moreover, the volumetric activity in the hot spheres is not necessarily indicative of the volumetric activity that may be found in a patient. The conformation and size of the lesions can also be highly variable. These issues have been addressed by recent studies, demonstrating that the optimization of personalized dosimetry for patients treated with ^{90}Y TARE must involve quantitative analyses conducted under conditions that are as reproducible as possible and closest to the patient's reality. One group has very recently used a phantom that is slightly more refined than the NEMA/IEC with a compartment simulating the background and a liver cavity in which a hollow cylindrical insert is fixed in order to simulate a lesion.[40] In another laboratory, a "homemade" phantom was designed and constructed with gelatin inside in order to realistically simulate the biodistribution of microspheres in two compartments simulating radioembolized liver regions.[41] Another author presented a ^{90}Y quantification work in SPECT imaging by comparing the results obtained with a uniform cylindrical phantom, an NEMA/IEC NU2 phantom and an anthropomorphic liver/kidney "Kyoto" phantom.[42] The latter has a very high level of complexity and includes an insert of 1.8 L simulating the liver, two cavities for the kidneys, a high-density element that is supposed to reproduce the lumbar part of the spine and the possibility to place lesions of different sizes,

hot and cold, in three different positions. The development of these more advanced phantoms appears crucial for improving the methodology underlying these studies.

5 | CONCLUSIONS

This work evaluated the performances of the Philips Vereos SiPM-based PET/CT scanner in comparison with those of the PMT-based predecessor TF64 for ^{90}Y-PET imaging. Based on activity quantifications and dosimetric analyses of phantom data, no major differences were found between the scanners performances; still, statistical comparison showed slightly better results with the SiPM-based Vereos system. Furthermore, based on the results obtained on patients' data, we recommend imaging patients treated with ^{90}Y TARE on the Vereos PET/CT system and to reconstruct the image with a 2-mm voxel size combined with the application of a PSF correction. This optimized set of reconstruction parameters clearly leads to an improved personalized ^{90}Y-PET-based dosimetry.

ACKNOWLEDGMENTS

The author(s) would like to express their most sincere gratitude to the technologist and radiopharmacist teams of the nuclear medicine department for their constant efforts that made this work possible.

CONFLICT OF INTEREST

GV is consultant for Boston Scientific, supplier of the ^{90}Y glass microspheres (TheraSphere). Other authors have no relevant conflict of interest to disclose related to the content of this article.

FUNDING INFORMATION

The author(s) received no financial support for this work.

DATA AVAILABILITY STATEMENT

The data that support the findings of this study are available from the corresponding author, NT, upon reasonable request.

ORCID

Nicola Trotta https://orcid.org/0000-0002-0871-1822

REFERENCES

1. Belgian Cancer Registry, « Cancer Fact Sheet – Liver Cancer – ICD10 : C22. Cancer_Fact_Sheet_Livercancer_2016.pdf. Published online 2016. Accessed June 24, 2021. http://kankerregister.org/media/docs/CancerFactSheets/2016/Cancer_Fact_Sheet_Livercancer_2016.pdf
2. Vilgrain V, Pereira H, Assenat E, et al. Efficacy and safety of selective internal radiotherapy with yttrium-90 resin microspheres compared with sorafenib in locally advanced and inoperable hepatocellular carcinoma (SARAH): an open-label randomised controlled phase 3 trial. *Lancet Oncol*. 2017;18(12):1624-1636. https://doi.org/10.1016/S1470-2045(17)30683-6
3. Chow PKH, Gandhi M, Tan SB, et al. SIRveNIB: selective internal radiation therapy versus sorafenib in Asia-Pacific patients with hepatocellular carcinoma. *J Clin Oncol*. 2018;36(19):1913-1921. https://doi.org/10.1200/JCO.2017.76.0892
4. Ricke J, Sangro B, Amthauer H, et al. The impact of combining selective internal radiation therapy (SIRT) with sorafenib on overall survival in patients with advanced hepatocellular carcinoma: the SORAMIC trial palliative cohort. *Ann Oncol*. 2018;29:v110. https://doi.org/10.1093/annonc/mdy149.028
5. Murthy R, Nunez R, Szklaruk J, et al. Yttrium-90 microsphere therapy for hepatic malignancy: devices, indications, technical considerations, and potential complications. *Radiographics*. 2005;25(suppl 1):S41-S55. https://doi.org/10.1148/rg.25si055515
6. Cremonesi M, Chiesa C, Strigari L, et al. Radioembolization of hepatic lesions from a radiobiology and dosimetric perspective. *Front Oncol*. 2014;4:210. https://doi.org/10.3389/fonc.2014.00210
7. Garin E, Lenoir L, Rolland Y, et al. Dosimetry based on 99mTc-macroaggregated albumin SPECT/CT accurately predicts tumor response and survival in hepatocellular carcinoma patients treated with 90Y-loaded glass microspheres: preliminary results. *J Nucl Med*. 2012;53(2):255-263. https://doi.org/10.2967/jnumed.111.094235
8. Garin E, Tselikas L, Guiu B, et al. Personalised versus standard dosimetry approach of selective internal radiation therapy in patients with locally advanced hepatocellular carcinoma (DOSISPHERE-01): a randomised, multicentre, open-label phase 2 trial. *Lancet Gastroenterol Hepatol*. 2021;6(1):17-29. https://doi.org/10.1016/S2468-1253(20)30290-9
9. Ho S, Lau WY, Leung TW, Chan M, Johnson PJ, Li AK. Clinical evaluation of the partition model for estimating radiation doses from yttrium-90 microspheres in the treatment of hepatic cancer. *Eur J Nucl Med*. 1997;24(3):293-298. https://doi.org/10.1007/BF01728766
10. Ho S, Lau WY, Leung TW, et al. Tumour-to-normal uptake ratio of 90Y microspheres in hepatic cancer assessed with 99Tcm macroaggregated albumin. *Br J Radiol*. 1997;70(836):823-828. https://doi.org/10.1259/bjr.70.836.9486047
11. Salem R, Lewandowski RJ, Atassi B, et al. Treatment of unresectable hepatocellular carcinoma with use of 90Y microspheres (TheraSphere): safety, tumor response, and survival. *J Vasc Interv Radiol, JVIR*. 2005;16(12):1627-1639. https://doi.org/10.1097/01.RVI.0000184594.01661.81
12. Shen S, DeNardo GL, Yuan A, DeNardo DA, DeNardo SJ. Planar gamma camera imaging and quantitation of yttrium-90 bremsstrahlung. *J Nucl Med*. 1994;35(8):1381-1389.
13. Elschot M, Nijsen JFW, Dam AJ, de Jong HWAM. Quantitative evaluation of scintillation camera imaging characteristics of isotopes used in liver radioembolization. *PLoS One*. 2011;6(11):e26174. https://doi.org/10.1371/journal.pone.0026174
14. Yue J, Mauxion T, Reyes DK, et al. Comparison of quantitative Y-90 SPECT and non-time-of-flight PET imaging in post-therapy radioembolization of liver cancer. *Med Phys*. 2016;43(10):5779. https://doi.org/10.1118/1.4962472
15. Porter CA, Bradley KM, Hippeläinen ET, Walker MD, McGowan DR. Phantom and clinical evaluation of the effect of full Monte Carlo collimator modelling in post-SIRT yttrium-90 bremsstrahlung SPECT imaging. *EJNMMI Res*. 2018;8(1):7. https://doi.org/10.1186/s13550-018-0361-0
16. Lhommel R, Goffette P, Van den Eynde M, et al. Yttrium-90 TOF PET scan demonstrates high-resolution biodistribution after liver SIRT. *Eur J Nucl Med Mol Imaging*. 2009;36(10):1696. https://doi.org/10.1007/s00259-009-1210-1

17. Pasciak AS, Bourgeois AC, McKinney JM, et al. Radioembolization and the dynamic role of (90)Y PET/CT. *Front Oncol*. 2014;4:38. https://doi.org/10.3389/fonc.2014.00038
18. Attarwala AA, Molina-Duran F, Büsing KA, et al. Quantitative and qualitative assessment of yttrium-90 PET/CT imaging. *PLoS One*. 2014;9(11):e110401. https://doi.org/10.1371/journal.pone.0110401
19. Tapp KN, Lea WB, Johnson MS, Tann M, Fletcher JW, Hutchins GD. The impact of image reconstruction bias on PET/CT 90Y dosimetry after radioembolization. *J Nucl Med*. 2014;55(9):1452-1458. https://doi.org/10.2967/jnumed.113.133629
20. D'Arienzo M. Emission of β+ particles via internal pair production in the 0+ – 0+ transition of 90Zr: historical background and current applications in nuclear medicine imaging. *Atoms*. 2013;1(1):2-12. https://doi.org/10.3390/atoms1010002
21. van Elmbt L, Vandenberghe S, Walrand S, Pauwels S, Jamar F. Comparison of yttrium-90 quantitative imaging by TOF and non-TOF PET in a phantom of liver selective internal radiotherapy. *Phys Med Biol*. 2011;56(21):6759-6777. https://doi.org/10.1088/0031-9155/56/21/001
22. Willowson KP, Tapner M, QUEST Investigator Team, Bailey DL. A multicentre comparison of quantitative (90)Y PET/CT for dosimetric purposes after radioembolization with resin microspheres: the QUEST Phantom Study. *Eur J Nucl Med Mol Imaging*. 2015;42(8):1202-1222. https://doi.org/10.1007/s00259-015-3059-9
23. ICW-3000™ Water Purification System – Other Products. Accessed September 28, 2021. https://www.merckmillipore.com/BE/en/product/ICW-3000-Water-Purification-System,MM_NF-C85500
24. Surti S, Kuhn A, Werner ME, Perkins AE, Kolthammer J, Karp JS. Performance of Philips Gemini TF PET/CT scanner with special consideration for its time-of-flight imaging capabilities. *J Nucl Med*. 2007;48(3):471-480.
25. Zhang J, Maniawski P, Knopp MV. Performance evaluation of the next generation solid-state digital photon counting PET/CT system. *EJNMMI Res*. 2018;8(1):97. https://doi.org/10.1186/s13550-018-0448-7
26. Walrand S, Hesse M, Jamar F, Lhommel R. The origin and reduction of spurious extrahepatic counts observed in 90Y non-TOF PET imaging post radioembolization. *Phys Med Biol*. 2018;63(7):075016. https://doi.org/10.1088/1361-6560/aab4e9
27. Snyder DL, Miller MI. The use of sieves to stabilize images produced with the EM algorithm for emission tomography. *IEEE Trans Nucl Sci*. 1985;32:3864-3872.
28. Golla S, Lammertsma A, Boellaard R. Performance of the resolution recovery method on the ingenuity PET/CT. *J Nucl Med*. 2015;56(suppl 3):1836-1836.
29. Hudson HM, Larkin RS. Accelerated image reconstruction using ordered subsets of projection data. *IEEE Trans Med Imaging*. 1994;13(4):601-609. https://doi.org/10.1109/42.363108
30. Morey AM, Kadrmas DJ. Effect of varying number of OSEM subsets on PET lesion detectability. *J Nucl Med Technol*. 2013;41(4):268-273. https://doi.org/10.2967/jnmt.113.131904
31. Soret M, Bacharach SL, Buvat I. Partial-volume effect in PET tumor imaging. *J Nucl Med*. 2007;48(6):932-945. https://doi.org/10.2967/jnumed.106.035774
32. Kao YH, Steinberg JD, Tay YS, et al. Post-radioembolization yttrium-90 PET/CT – Part 1: Diagnostic reporting. *EJNMMI Res*. 2013;3(1):56. https://doi.org/10.1186/2191-219X-3-56
33. Gulec SA, Mesoloras G, Stabin M. Dosimetric techniques in 90Y-microsphere therapy of liver cancer: the MIRD equations for dose calculations. *J Nucl Med*. 2006;47(7):1209-1211.
34. Weber M, Lam M, Chiesa C, et al. EANM procedure guideline for the treatment of liver cancer and liver metastases with intra-arterial radioactive compounds. *Eur J Nucl Med Mol Imaging*. 2011;38:1393-1406. https://doi.org/10.1007/s00259-021-05600-z. Published online February 11, 2022.
35. Accorsi R, Adam LE, Werner ME, Karp JS. Optimization of a fully 3D single scatter simulation algorithm for 3D PET. *Phys Med Biol*. 2004;49(12):2577-2598. https://doi.org/10.1088/0031-9155/49/12/008
36. Ye J, Song X, Hu Z. Scatter correction with combined single-scatter simulation and Monte Carlo simulation for 3D PET. In: 2014 IEEE Nuclear Science Symposium and Medical Imaging Conference (NSS/MIC). 2014:1-3. https://doi.org/10.1109/NSSMIC.2014.7431033
37. Goedicke A, Berker Y, Verburg FA, Behrendt FF, Winz O, Mottaghy FM. Study-parameter impact in quantitative 90-yttrium PET imaging for radioembolization treatment monitoring and dosimetry. *IEEE Trans Med Imaging*. 2013;32(3):485-492. https://doi.org/10.1109/TMI.2012.2221135
38. Scott NP, McGowan DR. Optimising quantitative 90Y PET imaging: an investigation into the effects of scan length and Bayesian penalised likelihood reconstruction. *EJNMMI Res*. 2019;9(1):40. https://doi.org/10.1186/s13550-019-0512-y
39. Duan H, Khalaf MH, Ferri V, et al. High quality imaging and dosimetry for yttrium-90 (90Y) liver radioembolization using a SiPM-based PET/CT scanner. *Eur J Nucl Med Mol Imaging*. 2021;48(8):2426-2436. https://doi.org/10.1007/s00259-021-05188-4
40. D'Arienzo M, Pimpinella M, Capogni M, et al. Phantom validation of quantitative Y-90 PET/CT-based dosimetry in liver radioembolization. *EJNMMI Res*. 2017;7(1):94. https://doi.org/10.1186/s13550-017-0341-9
41. Kao YH, Luddington OS, Culleton SR, Francis RJ, Boucek JA. A gelatin liver phantom of suspended 90Y resin microspheres to simulate the physiologic microsphere biodistribution of a postradioembolization liver. *J Nucl Med Technol*. 2014;42(4):265-268. https://doi.org/10.2967/jnmt.114.145292
42. Gnesin S, Leite Ferreira P, Malterre J, Laub P, Prior JO, Verdun FR. Phantom validation of Tc-99m absolute quantification in a SPECT/CT commercial device. *Comput Math Methods Med*. 2016;2016:4360371. https://doi.org/10.1155/2016/4360371

How to cite this article: Trotta N, Collette B, Mathey C, et al. Comparison of PMT-based TF64 and SiPM-based Vereos PET/CT systems for ^{90}Y imaging and dosimetry optimization: A quantitative study. *Med Phys*. 2022;1-16. https://doi.org/10.1002/mp.15880